Chemical Engineering Science 297 (2024) 120290

Contents lists available at ScienceDirect

Chemical Engineering Science

journal homepage: www.elsevier.com/locate/ces

An optimized hybrid battery pack with high energy density and high safety

Wendi Mo [a], Yiting Lin [a], Jiahui Li [b], Cheng Lian [a,b,*], Honglai Liu [a,b]

[a] State Key Laboratory of Chemical Engineering and Shanghai Engineering Research Center of Hierarchical Nanomaterials, School of Chemical Engineering, East China University of Science and Technology, Shanghai 200237, China
[b] School of Chemistry and Molecular Engineering, East China University of Science and Technology, Shanghai 200237, China

ARTICLE INFO

Keywords:
Lithium-ion battery
Hybrid battery pack
Battery thermal management
Air cooled condition

ABSTRACT

As traditional battery systems, lithium iron phosphate (LFP) batteries have better safety but lower energy density and nickel manganese cobalt oxide (NMC) batteries have higher energy density but poorer safety. In this work, we design a hybrid battery pack that has both higher energy density and higher battery safety. By analyzing the thermal properties of battery packs with aligned, staggered, and staggered arrangements, it can be concluded that the aligned arrangement has superior cooling efficiency and space-efficient optimization compared to the other arrangements, which have shorter flow paths to minimize air energy loss and reduce pressure drop. Notably, we design the optimal arrangement to avoid placing the NMC cells near the air outlet, to avoid NMC concentration, and to decentralize the LFP cells to reduce the relatively high maximum temperature and temperature difference. This hybrid battery pack is expected to give a boost to lithium-ion battery applications.

1. Introduction

With the swift progression in the field of electric vehicles (EVs), the lithium-ion batteries (LIBs), as the most promising energy source, have drawn great attention for their longer life, higher energy density, lower self-discharge rate (Yang et al., 2022; Zhang et al., 2021; Lai et al., 2022; Lu et al., 2013). However, improving energy density and thermal safety of LIBs is the most important challenge. The narrow optimal operating temperature range leads to the significant reduction of their cycle life at extreme operating temperatures. Battery thermal management system (BTMS) is an optimal approach to remedy these issues.

Multiple BTMS are dedicated to ensure the effective thermal control of LIBs, including air-based (Chen et al., 2021; Chen et al., 2017), water-based (Tang et al., 2019; Li et al., 2018), phase change material based (Guo et al., 2018; Wang et al., 2024; Li et al., 2023) cooling techniques. An efficient BTMS should ensure the working temperature within 20 °C to 40 °C and the temperature disparity less than 10 °C in the pack (Cao et al., 2021; Li et al., 2018; Fan et al., 2013). Among various cooling method, air-cooled is most wildly used with simplicity and low cost, but the efficiency is lower than other cooling techniques (Mahamud and Park, 2011; Chen et al., 2016).

A reasonable arrangement and spacing design of batteries can effectively improve the efficiency of air-cooled. The theory and methods in the field of lithium-ion battery air cooling are quite comprehensive, and these methods and conclusions have guiding significance for this work (Peng et al., 2019; Yang et al., 2015; Lu et al., 2018; Li et al., 2019; Peng et al., 2019; Ji et al., 2019). These methods can be beneficial in evaluating the system's response to transient conditions under dynamic operating scenarios, effectively enhancing the system's stability and accuracy. Fan et al. (Fan et al., 2019) explore the air-cooled performance of cylindrical battery packs revealing that the aligned battery pack not only has the lower average temperature but also consumes up to 23 % less energy loses than the cross packs. Liao et al. (Liao et al., 2019) find the average temperature of each battery decreases with increased longitudinal spacing, and the optimal design reduces the battery pack maximum temperature by 2.7 °C. Further studies indicate the uniformity of temperature is primarily affected by longitudinal pressure drop caused by longitudinal spacing (Kirad and Chaudhari, 2021; Mahamud and Park, 2011). Wang et al. (Wang et al., 2014) indicate that forced air-cooled is effective with an axisymmetric module structure, and Ji et al. (Ji et al., 2019) find geometric ratios arrangements to improve temperature uniformity, reducing the maximum temperature difference by 2.7 K.

To predict the effectiveness and performance of the BTMS, simulation calculation is an efficient and convenient method. Generally used battery models include the equivalent circuit model (ECM) (Wang et al., 2022; Jeon et al., 2023), single particle model (SPM) (Andrea et al., 2019; Tian et al., 2021), and pseudo-two-dimensional model (P2D) (Fuller et al., 1994; Doyle et al., 1993).

* Corresponding author.
E-mail address: liancheng@ecust.edu.cn (C. Lian).

https://doi.org/10.1016/j.ces.2024.120290
Received 20 January 2024; Received in revised form 29 March 2024; Accepted 23 May 2024
Available online 29 May 2024

Nomenclature

c_l	Lithium-ion concentration in the liquid phase (mol m^{-3})
c_s	Lithium-ion concentration in the solid phase (mol m^{-3})
$c_{s,max}$	Maximum lithium-ion density in active material (mol m^{-3})
$c_{s,surf}$	Surface concentration of Li^+ (mol m^{-3})
C_p	Thermal capacity (Jkg^{-1} K^{-1})
D_l	Lithium-ion electrolyte diffusion coefficient in the liquid phase (m^2 s^{-1})
D_s	Lithium-ion electrolyte diffusion coefficient in active material (m^2 s^{-1})
$D_{s,ref}$	Lithium-ion solid-phase diffusion coefficient at reference temperature (m^2 s^{-1})
$E_{a,D}$	Activation energy for diffusion (J mol^{-1})
$E_{a,R}$	Activation energy for reaction (J mol^{-1})
F	Faraday constant (96485C mol^{-1})
f	Mean molar activity coefficient
I	Imposed current density (A m^{-2})
i_l	Current density in liquid phase (A m^{-2})
i_s	Current density in solid phase (A m^{-2})
j_n	Reaction current density (A m^{-2})
j_0	Exchange current density (A m^{-2})
k_0	Constant for reaction rate ($m^{2.5}$ $mol^{-0.5}$ s^{-1})
$k_{0,ref}$	Constant for reaction rate at reference temperature ($m^{2.5}$ $mol^{-0.5}$ s^{-1})
Q_{rev}	Reversible entropic heat generation (J)
Q_{ohm}	Heat generation by ohmic losses (J)
Q_{rec}	Heat generation from reaction (J)
Q_{sum}	Sum of heat generated (J)
r	Particle radius variable (μm)
r_s	Radius of active material particle (μm)
R	Universal gas constant ($Jmol^{-1}$ K^{-1})
S_a	Specific surface area (m^{-1})
t_+	Li^+ transference number

Greek letters

α, β	Transfer coefficient
γ	Bruggeman exponent
ε_l	Volume fraction for liquid phase
ε_s	Volume fraction for solid phase
ν	Thermodynamics factor
η	Over potential (V)
ρ	Density (kg m^{-3})
σ	Electric conductivity
φ	Potential (V)

Subscripts and superscripts

0	Initial state
l	Liquid phase
s	Solid phase
amb	Ambient
eff	Effective value
ref	Reference value
SOC	State of charge

The ECM and the SPM can rapidly calculate macroscopic electrochemical behaviors, but neglect the intricate mass transport phenomena or thermal behavior within the LIBs. The P2D model, developed by Doyle and Newman (Fuller et al., 1994; Doyle et al., 1993), is one of the most precise models for describing the performance of LIBs. Based on the electrochemical equations, the P2D model reveals the chemical and physical characteristics of the LIBs. In our work, the P2D model is utilized to accurately predict the hybrid battery pack's electrical, chemical, and thermal behavior.

Nickel manganese cobalt oxide (NMC) and lithium iron phosphate (LFP) batteries are the mainstream batteries in the EVs market (Deng et al., 2020; Wu et al., 2019). However, they both have obvious disadvantages limiting their application. On the one hand, NMC batteries have thermal safety hazards and higher cost (Sato, 2000; Zhang et al., 2022). On the other hand, LFP batteries have lower energy density and the inaccurate SOC estimation (Chen et al., 2018; Farmann and Sauer, 2017). Previous research in hybrid battery systems, including combinations of LIBs with lead-acid batteries (Münderlein et al., 2020; Thien et al., 2022) and LIBs with supercapacitors (Hui and Minghai, 2021; Mesbahi et al., 2021), demonstrates the potential of these systems to leverage the strengths of each technology. These hybrid systems aim to optimize energy density, power output, safety, and lifespan, showcasing the wide-ranging possibilities for enhancing battery technology. In this work, a specific BTMS for a hybrid battery pack has been developed to enhance energy density with NMC and confirm LIBs' safety with LFP. This hybrid battery pack synergistically combines the distinct advantages of two battery types: the LFP batteries, known for their safety and cost-effectiveness, and the NMC batteries, recognized for their high performance. Building upon previous studies on hybrid battery packs (Münderlein et al., 2020; Li et al., 2021), we employ a SOC estimation and coordination method that accurately reflects the overall accurate SOC of the entire hybrid battery pack (Wang et al., 2023). The P2D model is used to accurately predict the hybrid battery pack's electrical, chemical, and thermal behavior. The three-dimensional model of 18,650 battery is used comprehensively analyze the influencing factors of the hybrid battery arrangement. Our objective is to conduct comprehensive research into potential improvements and optimizations aimed at enhancing the cooling performance of hybrid batteries under air-cooled conditions. In parallel, our proposed theoretical model endeavors to extend the range of thermal management strategies explored, integrating a variety of technologies and external factors to achieve a more effective thermal regulation of hybrid batteries.

2. Models and methods

2.1. Electrochemical model

To explore the thermal and electrochemical properties of hybrid batteries in different environments, a heat transfer and fluid flow model are developed to simulate the temperature changes of hybrid battery packs in air conditions and designed a SOC estimation and coordination method to confront and describes temperature changes precisely.

The P2D model is the primary electrochemical model in this work, as shown in Fig. 1A. Since the P2D model assumes a uniform distribution of electrode active material pores/electrolyte within the electrode, Li-ion battery is simplified to a one-dimensional model with three parts: the negative electrode, the positive electrode, and the separator. The P2D model can dynamically simulate the electrochemical performance of batteries under various operational conditions, including changes in voltage, current, temperature, and lithium-ion concentration distribution. The model describes the multi-physical processes inside the battery using a set of partial differential equations (PDEs), covering electron and ion conduction, electrochemical reactions, mass transport, and thermal conduction. This model is particularly well-suited for studying battery behavior during charging and discharging, as well as under dynamic conditions such as temperature variations. The following assumptions are made in the P2D model: (a) chemical reactions occur at the electrodes; (b) the active particle material is presumed to have a spherical configuration; (c) the electric double layer is not considered.

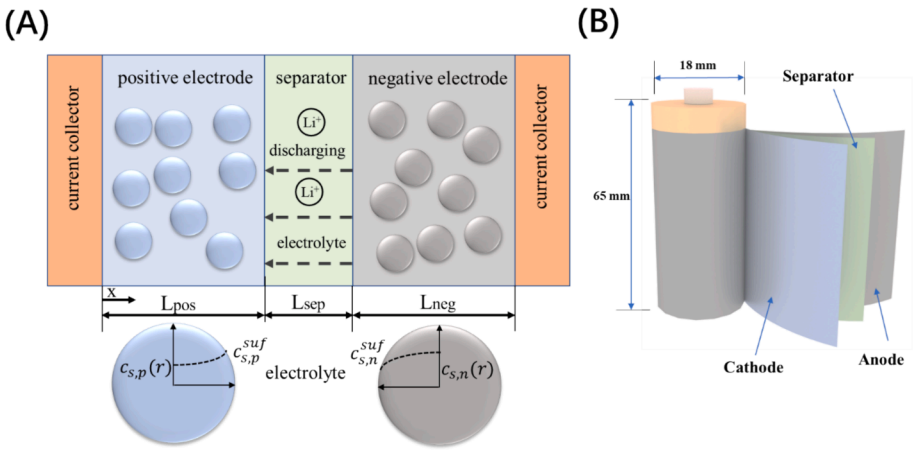

Fig. 1. Battery models, (A) P2D electrochemical model; (B) 18,650 battery cylindrical battery model.

2.1.1. Charge transfer

The sum of current density in the liquid phase and the solid phase equals the current density in the external circuit:

$$I = i_s + i_l \tag{1}$$

$$\nabla I = \nabla i_s + \nabla i_l \tag{2}$$

The connection between current density and electrochemical reaction current density is as follows:

$$\nabla i_l = S_a j_n \tag{3}$$

$$\nabla i_s = -S_a j_n \tag{4}$$

Where, S_a according to the spherical particle model is expressed as follows:

$$S_a = \frac{3\varepsilon_s}{r_s} \tag{5}$$

Where, j_n represents the local charge transfer current density described by the Butler-Volmer equation. This equation establishes a connection between concentration changes and current on the surface of electrode active particles:

$$j_n = j_0 \left[exp\left(\frac{\alpha F\eta}{RT}\right) - exp\left(-\frac{\beta F\eta}{RT}\right) \right] \tag{6}$$

Where, j_0 is the exchange current density, reflecting the absolute rate of oxidation and reduction reactions at equilibrium potential, which is related to the constant for reaction rate and concentration. The particle surface overpotential η is expressed as follows:

$$\eta = \varphi_s - \varphi_l - U_{eq} \tag{7}$$

Where, φ_l and φ_s are respectively the liquid and solid phase potentials, U_{eq} is the open circuit voltage of the electrode, which is the function of $c_{s,surf}$ and T. The current density in solid phase is related to conductivity, which can be expressed with Ohm's law:

$$i_s = -\sigma_s^{eff} \nabla \varphi_s \tag{8}$$

The liquid phase lithium-ion current densities are as follows:

$$i_l = \sigma_l^{eff} [-\nabla \varphi_l + \frac{2RT}{F}(1 + \frac{\partial lnf}{\partial lnc_l}(1 - t_+)\nabla lnc_l)] \tag{9}$$

This equation expresses the effect of concentration diffusion and electromigration on the liquid phase current density.

2.1.2. Mass transfer

Li-ion diffusion behaviors in spherical active particles be elucidated by the Fick's second law:

$$\frac{\partial c_s}{\partial t} = \frac{1}{r^2}\frac{\partial}{\partial r}\left(D_s r^2 \frac{\partial c_s}{\partial r}\right) \tag{10}$$

The lithium-ion conservation in electrolyte phase is given by the following formula:

$$\varepsilon_l \frac{\partial c_l}{\partial t} = \nabla\left(D_l^{eff} \nabla c_l\right) + S_a(1 - t_+) j_0 \tag{11}$$

This equation describes Li-ion concentration changes using divergence to express diffusion and transport effects.

2.1.3. Heat generation

Considering heat capacity and heat transfer effects, the main heat sources are divided into three parts: irreversible reaction heat (Q_{rea}), ohmic heat (Q_{ohm}) and reversible entropic heat (Q_{rev}):

$$\rho C_p \frac{\partial T}{\partial t} - k\nabla^2 T = Q_{rea} + Q_{rev} + Q_{ohm} \tag{12}$$

The heat generated by irreversible reactions is linked to both the overpotential and the density of the reaction current:

$$Q_{rea} = S_a j \eta \tag{13}$$

The Q_{rev} is expressed as follows:

$$Q_{rev} = S_a j_n T \frac{\Delta S}{F} = S_a j_n T \frac{dU}{dT} \tag{14}$$

The Q_{ohm} generated in the solid and liquid phases is expressed as follows:

$$Q_{ohm} = -i_s \nabla \varphi_s - i_l \nabla \varphi_l \tag{15}$$

2.1.4. Coefficient correction

Conductivity and liquid phase mass transfer coefficient are amended by Bruggeman theorem:

$$\sigma_s^{eff} = \sigma_s \varepsilon_s^{\gamma} \tag{16}$$

$$\sigma_l^{eff} = \sigma_l \varepsilon_l^{\gamma} \tag{17}$$

$$D_l^{eff} = D_l \varepsilon_l^{\gamma} \tag{18}$$

Where γ represents the Bruggeman porosity exponent, assigned a value of 1.5 in our work.

2.1.5. Battery thermodynamic properties

Fig. 1B illustrates the three-dimensional model of a single battery, constructed based on the following assumptions: the heat generated

during the discharge is evenly distributed with radial/axial anisotropy of the heat transfer coefficient. Additionally, the effects of thermal variations on material properties are neglected, and thermal radiation is not considered. The total heat production of the batteries is expressed as follows:

$$Q_{sum}=\frac{\left[\left(Q_{rea,neg}L_{neg}+Q_{\mathrm{rev}}L_{\mathrm{neg}}\right)+\left(Q_{rea,pos}L_{pos}+Q_{\mathrm{rev,pos}}L_{\mathrm{pos}}\right)+\sum Q_{\mathrm{ohm},i}L_i\right]A}{\pi R_{\mathrm{batt}}^2} \tag{19}$$

The thermal conductivity is anisotropic, so the thermal conductivity in the radial and axial directions needs to be calculated relatively (Chiew et al., 2019; Chen et al., 2006). The following equation defines the radial thermal conductivity:

$$k_{battery,r}=\frac{\sum L_i}{\sum L_i/k_i} \tag{20}$$

Where, L_i is the length of electrode and separator; k_i is the thermal conductivity of the electrode and separator. The following equation defines the axial thermal conductivity:

$$k_{battery,ang}=\frac{\sum L_i k_i}{\sum L_i} \tag{21}$$

The heat production equation for a cylindrical battery is as follows:

$$\rho C_p\frac{\partial T}{\partial t}-\nabla(k\nabla T)=Q_{sum} \tag{22}$$

Where, C_p is the battery heat capacity, k is the anisotropic thermal conductivity. The heat transfer equation at the battery surface is expressed as follows:

$$-k\left(\frac{\partial T}{\partial n}T\right)=h(T_{amb}-T) \tag{23}$$

Where, $\partial T/\partial n$ is directional derivative of temperature; h is convective heat transfer coefficient; T_{amb} is temperature in ambient environment.

2.1.6. Heat transfer and fluid flow model

The flow field elucidated by the Navier-Stokes(N-S) equations:

$$\frac{\partial \rho}{\partial t}+\nabla\rho u=0 \tag{24}$$

$$\rho\left(\frac{\partial u}{\partial t}+u\nabla u\right)=-\nabla p+\nabla\{\mu[(\nabla u+\nabla u)^T-\frac{2}{3}\mu(\nabla u)I\}+F \tag{25}$$

Where, ρ is the fluid mass density, u is the velocity of flow,p is the fluid static pressure, μ is the fluid's viscosity, I is the identity matrix, F is the external forces on fluid. Generally, the boundary condition is $u = 0$.

N-S equations reflect that the behavior of the fluid in the model can be predicted when initial values defined. In our work, we calculate the steady state process of fluid heat transfer, and the following equation describes the fluid temperature change:

$$\rho C_p\frac{\partial T}{\partial t}+\rho C_p u\nabla T=\nabla(k\nabla T)+Q \tag{26}$$

Where, C_p is the heat capacity, Q is the external heat source.

2.2. Model parameters

The model parameters include constant parameters and variable parameters influenced by temperature or concentration. The parameters for the two types of batteries used in this work are shown in Table 1 and Table 2, with data from the references (Maheshwari et al., 2016; Wang et al., 2021; Lyu et al., 2020; Xu et al., 2014; Ren et al., 2022).

Constant for reaction rate is calculated by the Arrhenius formula.

Table 1
The main parameters in LFP model.

Parameters	Negative electrode	Separator	Positive electrode
ε_s	0.51	n/a	0.81
ε_l	0.46	0.4	0.18
$L(\mu m)$	56	16	86
$r_p(\mu m)$	4.5	n/a	5.75
$c_{s,0}\left(mol/m^3\right)$	15,685	n/a	228.06
$c_{s,max}\left(molm^{-3}\right)$	31,370	n/a	22,806
$c_{l,0}\left(molm^{-3}\right)$	1000	1000	1000
α	0.5	n/a	0.5
β	0.5	n/a	0.5
$D_{s,ref}\left(m^2s^{-1}\right)$	3.9×10^{-14}	1.3×10^{-10}	2.2×10^{-14}
$E_{aD}\left(kJmol^{-1}\right)$	35	n/a	35
$E_{aR}\left(kJmol^{-1}\right)$	20	n/a	20
$\sigma_s\left(Sm^{-1}\right)$	100	0.771	6
$k_{0,ref}\left(m^{2.5}mol^{-0.5}s^{-1}\right)$	2×10^{-11}	n/a	1×10^{-9}
$k(W/m{\cdot}K)$	4.21	1.21	0.27
γ	1.5	1.5	1.5
$\rho\left(kg/m^3\right)$	1861	1043	2300
t_+	0.363	0.363	0.363
$C_p(J/kg{\cdot}K)$	1437	1978	1260

Table 2
The main parameters in NMC model.

Parameters (unit)	Negative electrode	Separator	Positive electrode
ε_s	0.67	n/a	0.685
ε_l	0.3	n/a	0.266
$L(\mu m)$	70	32	52.5
$r_p(\mu m)$	12.5	n/a	8
$c_{s,0}\left(mol/m^3\right)$	21,910	n/a	13,779
$c_{s,max}\left(molm^{-3}\right)$	31,370	n/a	49,388
$c_{l,0}\left(molm^{-3}\right)$	1000	1000	1000
α	0.5	n/a	0.5
β	0.5	n/a	0.5
$D_{s,ref}\left(m^2s^{-1}\right)$	3.9×10^{-14}	n/a	1.3×10^{-13}
$E_{aD}\left(kJmol^{-1}\right)$	35	n/a	20
$E_{aR}\left(kJmol^{-1}\right)$	30	n/a	30
$\sigma_s\left(Sm^{-1}\right)$	100	n/a	3.8
$k_{0,ref}\left(m^{2.5}mol^{-0.5}s^{-1}\right)$	2×10^{-11}	n/a	5×10^{-11}
$k(W/m{\cdot}K)$	1.04	1	1.48
γ	1.5	1.5	1.5
$\rho\left(kg/m^3\right)$	1600	492	3000
t_+	0.363	0.363	0.363
$C_p(J/kg{\cdot}K)$	1095	1883	1016

$$k_0=k_{0,ref}\exp\left[\frac{E_{aR}}{R}\left(\frac{1}{T_{ref}}-\frac{1}{T}\right)\right] \tag{27}$$

Lithium-ion electrolyte diffusion coefficient related to temperature can also be described by the following Arrhenius formula:

$$D_0=D_{0,ref}exp\left[\frac{E_{aD}}{R}\left(\frac{1}{T_{ref}}-\frac{1}{T}\right)\right] \tag{28}$$

The solid phase equilibrium potential is related to temperature by the following equation:

$$U_{eq}=U_{ocv+}\frac{dU}{dT}\left(T-T_{ref}\right) \tag{29}$$

Where U_{eq} (the electrode voltage) and dU/dT (the entropy change) are related to the battery SOC. The concentration SOC of the active material particles is defined as follows:

$$SOC=\frac{c_s}{c_{s,max}} \tag{30}$$

The open circuit voltage (U_{ocv}) of the graphite electrode and entropy change (dU/dT) is used from references, as shown in Fig. 2.

2.2.1. Parameters of LFP

The values of U_{ref} and dU/dT of LFP batteries are related to the SOC as follows:

$$U_{ocv} = 3.399 - 1.239\exp\Big(-7.903(1-\mathrm{soc})^{0.3821} - (-3.644 \times 10^{-10})\exp\Big(21.12(1-\mathrm{soc})^{30.37}\Big) + \Big(8.249 \times 10^{-12}\exp\Big(22.39(1-\mathrm{soc})^{1.56}\Big) \tag{31}$$

$$dU/dT = -0.35376\mathrm{soc}^8 + 1.3902\mathrm{soc}^7 - 2.2585\mathrm{soc}^6 + 1.9635soc^5 - 0.98716soc^4 + 0.28857soc^3 - 0.046272\mathrm{soc}^2 + 0.0032158\mathrm{soc} - 1.9186 \times 10^{-5} \tag{32}$$

The conductivity and transfer coefficient of liquid phase Li^+ as a function of temperature and concentration are described as follows:

$$\sigma_l(c_l,T) = 1.2544c_l \times 10^{-4}\big(-8.2488 + 0.053248T - 2.9871 \times 10^{-5}T^2 + 0.26235c_l - 9.3063 \times 10^{-3}c_lT + 8.069 \times 10^{-6}c_lT^2 + 0.22002c_l^2 - 1.765 \times 10^{-4}c_l^2T\big)^2 \tag{33}$$

$$D_l(c_l,T) = 4 \times 10^{-4} \times 10^{-4.43-\frac{54}{T-229-0.005c_2}} - 2.2 \times 10^{-4}c_l \tag{34}$$

$$\nu(c_l,T) = 0.601 - 0.24 \times (0.001c_l)^{0.5} + 0.982 \times [1 - 0.0052 \times (T - 294)] \times (0.001c_l)^{1.5} \tag{35}$$

2.2.2. Parameters of NMC

The values of U_{ref} and dU/dT of NMC batteries are related to the SOC as follows:

$$U_{ocv} = -320.7\,soc^8 + 1138\,soc^7 - 1629\,soc^6 + 1193\,soc^5 - 460.3\,soc^4 + 81.24\,soc^3 - 0.9206\,soc^2 - 2.304\,\mathrm{soc} + 4.387 \tag{36}$$

$$dU/dT = 0.08398soc^8 - 0.354soc^7 + 0.5917soc^6 - 0.4988soc^5 + 0.2225soc^4 - 0.05003soc^3 + 0.004758soc^2 - 0.0002091soc + 3.239 \times 10^{-5} \tag{37}$$

The conductivity and transfer coefficient of liquid phase Li^+ as a function of temperature and concentration are described as follows:

$$\sigma_l(c_l,T) = 10^{-4}c_l \times (-8.2488 + 0.053248T - 0.0002987T^2 + 0.26235 \times 10^{-3}c_l - 0.009063 \times 10^{-3}c_lT + 0.000008069e^{-3}c_lT^2 + 0.22002 \times 10^{-6}c_l^2 - 0.0001765e^{-6}c_l^2T)^2 \tag{38}$$

$$D_l(c_l,T) = 10^{\left(-4.43-\frac{54}{T-5\times10^{-3}c_l-229} - 0.22 \times 10^{-3}c_l\right)^{-4}} \tag{39}$$

$$\nu(c_l,T) = 1.06 \times [0.601 - 0.24 \times 10^{-2}c_l^{0.5} + (-0.0051064T + 2.47894) \times (10^{-3}c_l)^{1.5}] \tag{40}$$

2.3. SOC coordination method

Fig. 3 illustrates the voltage–time profiles of the NMC and LFP batteries at different discharge rates (1C, 2C, 3C). In a parallel battery system, the discharge times of NMC batteries are shorter than that of LFP batteries, and the difference increases as the discharge rate increases.

To verify the feasibility of the hybrid battery discharge protocol, a comprehensive SOC window usage segment and a SOC coordination method to manage the SOC between different capacity batteries are designed. This approach involves mapping the upper and lower SOC limits of NMC batteries to the SOC range of the entire battery system, thus establishing a correlation between the SOC limits of the NMC batteries and the system's SOC range.

The easily estimable NMC can be used as a "benchmark" to define hybrid battery pack's working windows for the hybrid batteries and implement balancing control algorithms (Guan et al., 2023; Shuai et al., 2023).The results of their experiments proved that this approach can control the SOC estimation error for hybrid battery pack within approximately 1 %.

Inspired by this work and taking into account the existing hybrid design approaches for LFP and NMC batteries (Kim and Jung, 2018; Kim et al, 2019), a specific SOC working windows is defined for each battery type. Given the potential complexities in the BMS due to varying rates of capacity degradation, the working window is designated for NMC batteries from 0 to 0.9 and for LFP batteries from 0.1 to 1. This ensures that the operational capacities of both types of batteries are maintained upon reaching their degradation endpoints. On this basis, we implement high-power capacity balancing technology within the battery system as a means of regulating and balancing the SOC of the battery pack, thereby maintaining battery operation within the defined capacity windows.

Essentially, the 100 % SOC point of LFP cells is set as the battery

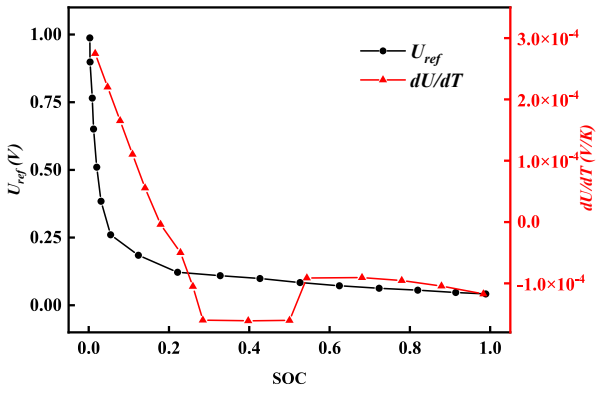

Fig. 2. U_{ref}And dU/dT of graphite electrode.

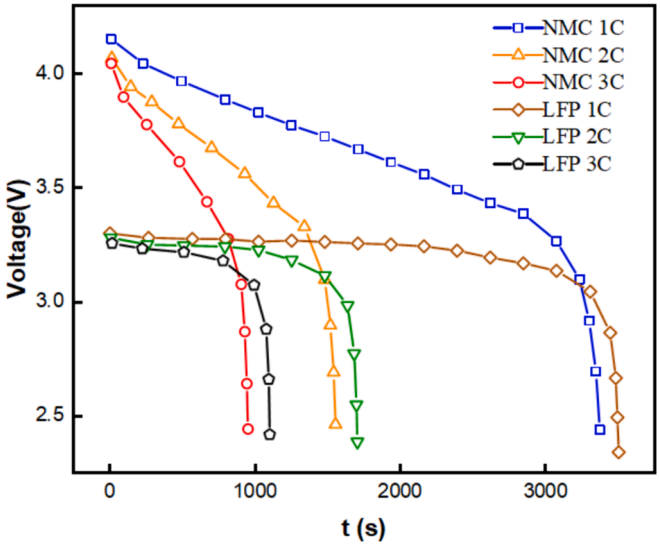

Fig. 3. Discharge curves of LFP and NMC battery.

pack's full charge point, while the 0 % SOC point of NMC batteries serves as the full discharge point, as shown in Fig. 4A. Consequently, the usable capacity of the battery pack cycles between the 0 % SOC of NMC and the 100 % SOC of LFP batteries.

The NMC battery is utilized as a standard to estimate the SOC of the hybrid battery pack due to the advantage of the significant variation in open-circuit voltage curve of the NMC battery. To align NMC battery's SOC estimation with the battery pack, the NMC battery's SOC connect the entire battery system's SOC, as shown follows:

$$SOC_{max,pack} = \frac{SOC_{max,NMC} - SOC_{min,NMC}}{SOC_{max,NMC}} \tag{41}$$

In this work, the SOC of the LFP battery has a range of 0.1–1, and of the NMC battery has a range of 0–0.9. Reserving a portion of the capacity ensures accurate application of the SOC estimation and method, even in cases where there is a significant difference in the rate of capacity fade in the hybrid battery pack. The lower and upper limits of the NMC battery can be set as 0 % and 90 %, respectively, and they are mapped to the SOC range of the battery system from 0 % to 100 %. According to the Eq. 41, when the NMC battery's SOC is 0 %, the battery pack's SOC is 0 %; when NMC battery's SOC is 45 %, the battery pack's SOC is 50 %; and when the NMC battery's SOC is 90 %, the battery pack's SOC is 100 %. On the other hand, LFP battery will be calibrated after each full charge, and the SOC will be estimated using a fuzzy estimation method.

The SOC estimation method for hybrid battery packs needs to be adjusted as the capacity fade. As the battery capacity degrades, the lower limit of LFP gradually opens up, ensuring the fully charged state of the LFP battery always corresponds to the highest $SOC_{max,NMC}$ (90 %) and the NMC depletion position corresponds to the low point $SOC_{min,LFP}$ (<=10 %) of the LFP battery, as shown in Fig. 4B.

The SOC coordination between hybrid batteries can be represented by:

$$\Delta SOC_{LFP} = \frac{\Delta SOC_{NMC} \times Q_{max,NMC}}{Q_{max,LFP}} \times h \tag{42}$$

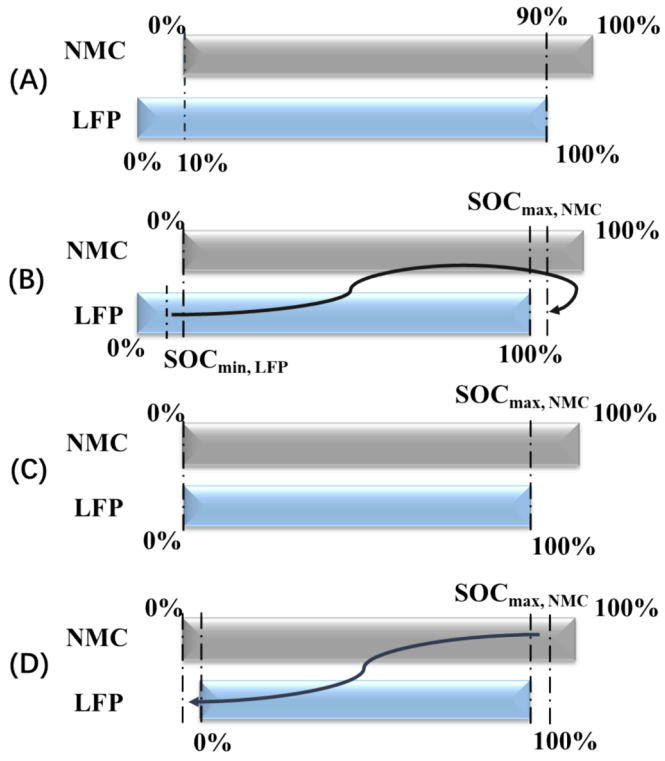

Fig. 4. SOC coordination method of LFP and NMC battery.

Where, Q_{LFP}, Q_{NMC} are the maximum capacities of the LFP battery and NMC battery, the variable h is the actual adjustment coefficient, ΔSOC_{LFP}, ΔSOC_{LFP} indicate the SOC adjustment method for the SOC changes of the two types of batteries.

As the capacity of the LFP battery further fades, Fig. 4C illustrates the lower limit of LFP battery is fully opened. As shown in Fig. 4D, with the capacity fading, the NMC battery with a larger capacity will provide charge to the smaller-capacity LFP battery to maximize the utilization of energy and deplete simultaneously.

2.4. Numerical methods

COMSOL Multiphysics is used to analyze the characteristic of a cylindrical (18650 type) hybrid battery pack in air-cooled with the heat dissipation model. The heat generation rate of the batteries is calculated by the electro-thermal coupled P2D model. Applied the heat generation rate to the three-dimensional thermal energy transfer mechanism can calculate the real-time temperature of batteries and correct the parameter of electrochemical model.

The calculation consists of two steps: initializing the current distribution to improve the convergence of subsequent solving process, and calculating with transient solvers. The user-controlled relative tolerance is 0.001, and the time step is the backward difference formula (BDF) method.

2.5. Model validation

Fig. 5 displays a close match between the simulation results (lines) and experimental data (symbols) of individual LFP and NMC batteries at different discharge rates and at 25 °C, indicating that the model can accurately simulate the actual discharge process. Fig. 5 indicates that the battery performance, both at high and low discharge rates, closely aligns with experimental results, which reflects the battery model's accuracy.

3. Results and discussion

This work focuses on cylindrical batteries, and employs a P2D model, a coupled heat transfers and fluid dynamics theory for numerical simulations. The theoretical framework and analytical methodologies are adapted to investigating hybrid batteries of varied geometric configurations and external factors.

3.1. Effect of hybrid batteries arrangement on pack temperature

Air-Cooled methodology is utilized in this work with a velocity of 0.1 m/s and a temperature at 298.15 K. The battery pack is composed of 12 LFP and 12 NMC batteries, with batteries of the same type connected in series. The distance between batteries is determined as 0.5 × R_{batt}, where R_{batt} represents the battery radius. To maintain the same battery distribution density, the centers of the batteries in the airflow direction are spaced by 2.5 times the battery radius (s = 2.5 × R_{batt}).

Fig. 6 shows three common air-cooled arrangements for LIBs, including the aligned, cross and staggered arrangement.

The thermal performance of different hybrid batteries arrangements at 2C are analyzed by simulating 6 different layouts for aligned and cross arrangements and 5 different layouts for staggered arrangement.

3.2. Aligned arrangement

Figs. 7 and 8 contrast the thermal behavior of battery packs with different layouts of aligned arrangement, indicating that Layout 3 and Layout 4 have relatively higher maximum temperatures (T_{max}) and temperature difference (ΔT). In Layout 3, the concentrated distribution of NMC batteries leads to a peak temperature exceeding 314 K at the outlet. In Layout 4, NMC batteries are segmented by LFP, which effectively prevents the heat accumulation effect in NMC batteries.

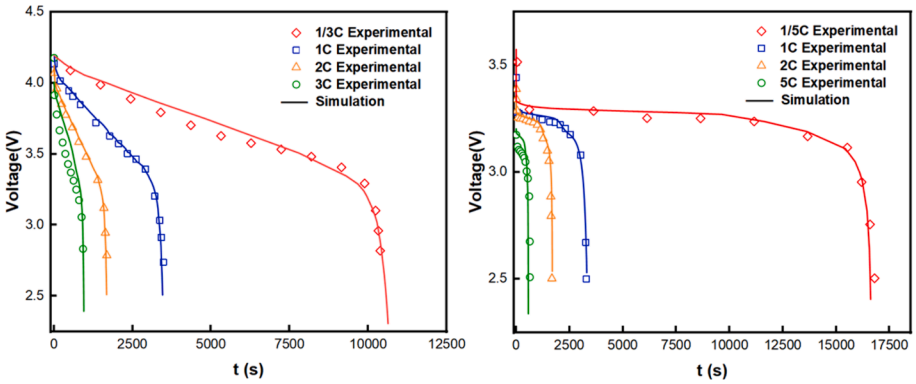

Fig. 5. The discharging curves of (A) LFP battery and (B) NMC battery. The symbols and lines correspond to experimental and simulated data.

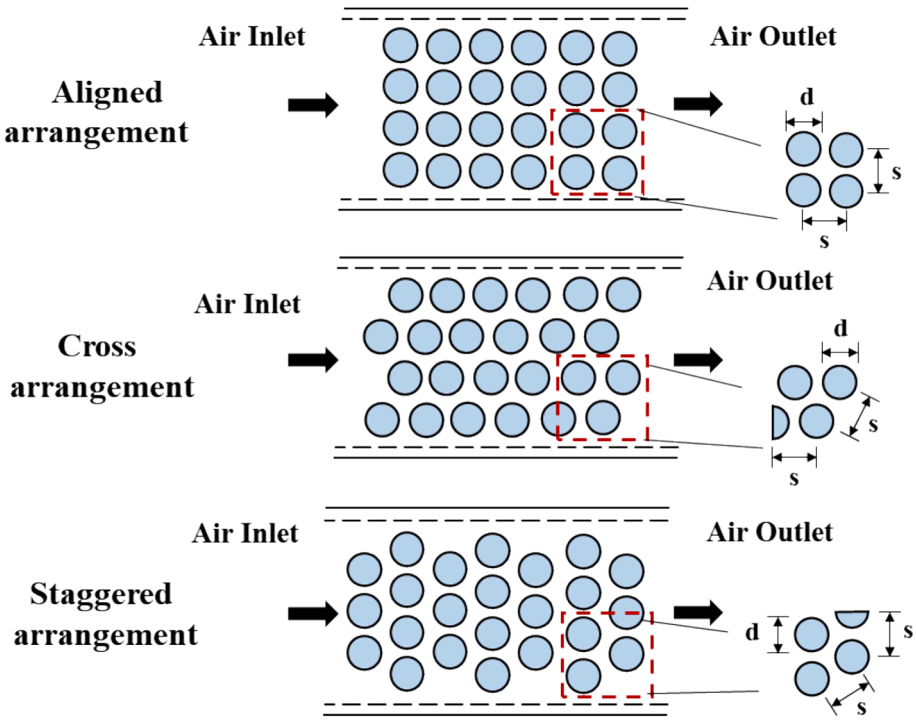

Fig. 6. Battery arrangements in air-cooled conditions.

Meanwhile, the airflow adjacent to the lateral sides of the channel is fast and cool, significantly lowering the temperature of the NMC batteries on the outer side, which results in a decrease of 1 K for both T_{max} and ΔT in Layout 4 compared to Layout 3. The Layout 3 and 4 have poor cooling performance, the NMC battery at the air outlet has the highest temperature, which suggests a significant safety risk with a high heat generation. Therefore, Layout 5 with NMC batteries at the front is adopted to explore the thermal effects in hybrid battery packs. Benefiting from the colder air near the inlet for enhanced cooling, NMC batteries at the front are cooled effectively. Simultaneously, despite the LFP batteries are exposed to warmer air, the risk of thermal runaway is low due to the LFP batteries' low heat generation rate. Layout 5 effectively mitigates the ΔT between batteries, resulting in a more balanced overall temperature distribution. However, the concentration of the high heat generation sources (NMC batteries) has potential dangers. In Layout 5, the NMC batteries' central area in the downward direction of the air has the T_{max}, which is the most susceptible to thermal runaway.

To avoid concentration of heat sources, we propose three types of discrete distributions. In Layout 1 and Layout 2, the batteries are arranged in rows, one after another. Results show both have similar T_{max}, but Layout 1 exhibits a smaller ΔT about 3 K. Because in Layout 1 the NMC batteries in the first row are directly cooled by air, and the NMC batteries in the third and fifth rows are flanked by colder LFP batteries. The high heat generation sources with low heat generation sources and avoids the possible localized high temperatures at the air outlet, realizing the effectively control of ΔT and T_{max} in Layout 1. In Layout 6, the batteries are spaced apart with different types of batteries dispersed in a discrete distribution. Thermal performance of Layout 6 is similar to Layout 2, indicating that the discrete distribution of batteries can effectively balance the T_{max} through different heat generation rates, but the key to reducing the ΔT is avoiding high heat-generating sources near the outlet.

In summary, Layout 1 effectively controls the maximum temperature, while Layout 5 achieves a more average temperature distribution across the battery pack.

3.3. Cross arrangement

Compared to the aligned arrangement, the flow path distribution of the air is changed in the cross arrangement. As shown in Figs. 9 and 10,

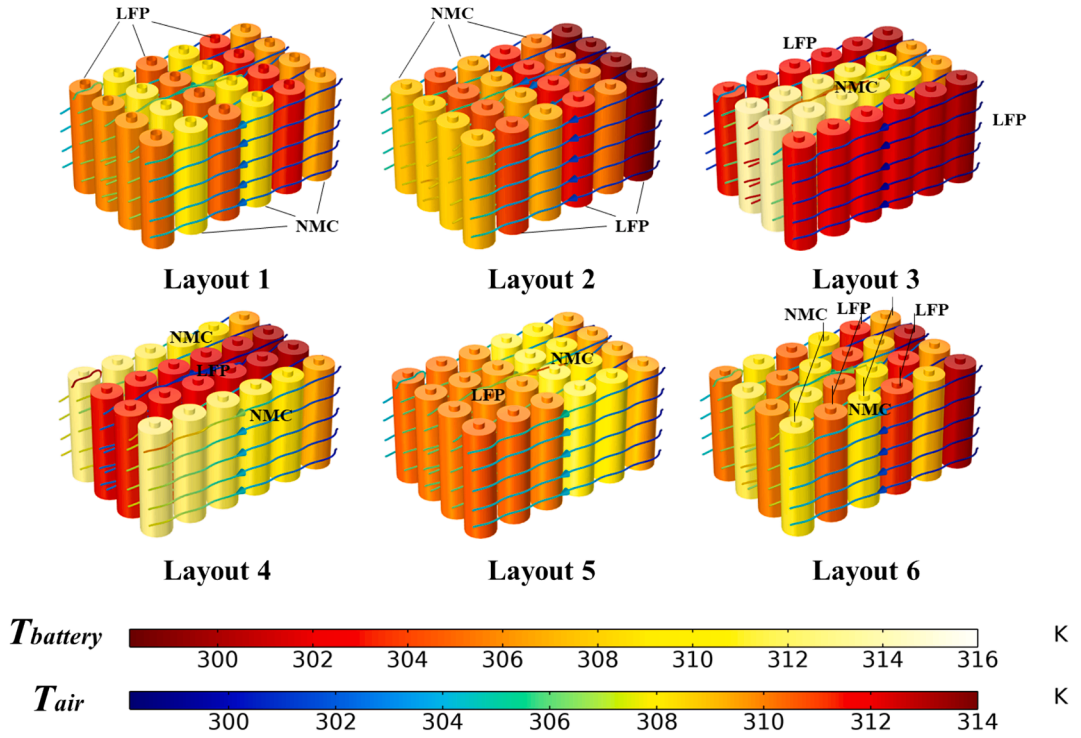

Fig. 7. Hybrid battery temperature distribution of aligned arrangement.

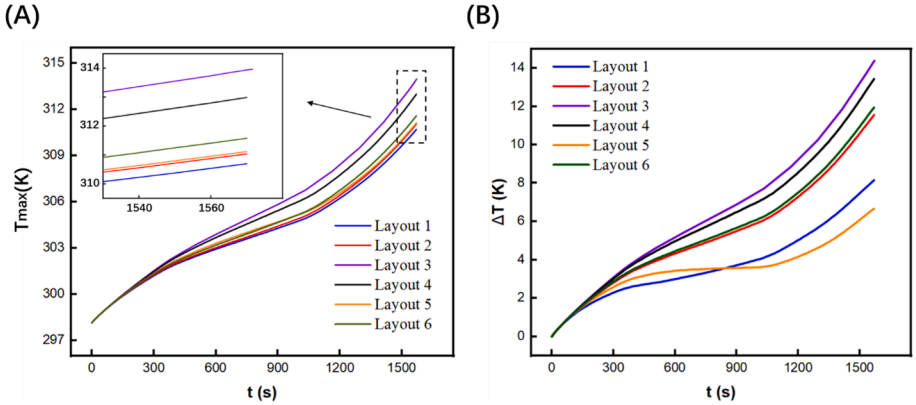

Fig. 8. Temperature-time graph curves of aligned arrangement in Layout 1 ~ 6, (A) maximum temperature (T_{max}) of battery system; (B) maximum temperature difference (ΔT) of battery system.

Layout 4 has the highest T_{max} and ΔT, and the results indicate that the T_{max} occurs inside the NMC batteries near the air outlet. Because positioning of NMC batteries at the air output, where they are devoid of any adjacent LFP batteries to balance temperature. Additionally, the concentration of heat in the middle section significantly raises the temperature of the air flowing through, further exacerbates the temperature rise in the NMC batteries. In Layout 5, arranging NMC batteries at the front, similar to the aligned arrangement, effectively balances the temperature within the hybrid battery pack. These layouts indicating that the inherent characteristics of the cross arrangement result in NMC batteries at the outlet not being surrounded by NMC batteries, which significantly elevates the potential for thermal runaway events.

The temperature of Layout 1, 2, and 6 is lower than Layout 3 and Layout 4, and higher than aligned arrangement. Layout 1 have the lowest T_{max}, emphasizing the significance of avoiding the placement of NMC batteries at the air outlet and adopting a discrete distribution method in preventing thermal runaway.

Cross arrangements can improve heat dissipation by creating more open spaces and airflow passages between the battery batteries, facilitating more efficient heat transfer. Notably, the increased distance between LFP and NMC batteries in cross arrangement compared to aligned arrangement leads longer heat transfer path between different battery types, impeding the capability of LFP batteries to contribute to the overall temperature regulation of the battery pack. Therefore, the effectiveness of air-cooled in a cross arrangement is noticeably inferior to that of an aligned arrangement. The flow paths are more direct and consistent in an aligned arrangement, ensuring that cooling air is evenly distributed across all battery batteries. In contrast, the cross arrangement disrupts the uniformity of the airflow paths, leading to uneven cooling effectiveness and consequently localized temperature variations.

3.4. Staggered arrangement

The staggered arrangement increases the contact area with the airflow, greatly enhances the convective strength. As shown in Figs. 11

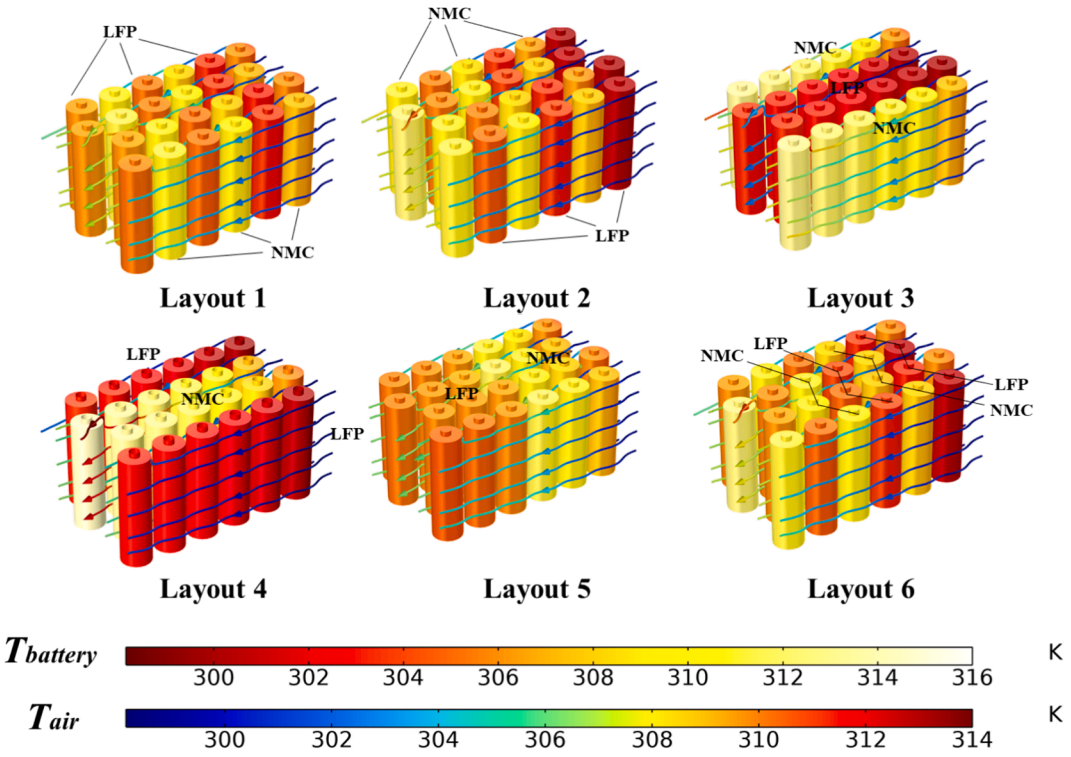

Fig. 9. Hybrid battery temperature distribution of cross arrangement.

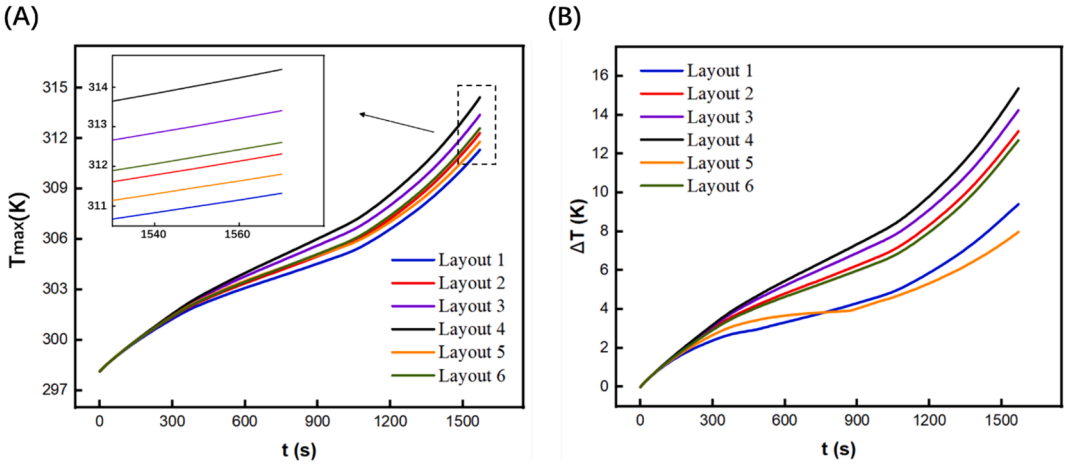

Fig. 10. Temperature-time graph curves of cross arrangement Layout 1 ~ 6, (A)maximum temperature (T_{max}) of battery system;(B) maximum temperature difference (ΔT) of battery system.

and 12, compared to the above arrangements Layout 3 effectively control T_{max} of the external NMC batteries. The performance of Layout 3 and 4 illustrates better cooling of the external batteries due to less resistance of the external air and less energy loss from the air. Layout 5 has the smallest T_{max} and ΔT among the layouts. Notably, during 900 s to 1000 s, ΔT of the battery pack does not increase but rather decreases, which indicates staggered arrangement improves the efficiency of heat transfer through air, facilitating the removal of heat from the system, particularly from the front NMC batteries during the mid-discharge phase.

Layout 1 and 2 reduce average temperature compared to the similar layouts of the previous two arrangements, because in the staggered arrangement hybrid battery pack has smaller battery distribution density and improved air heat transfer. Notably, Layout 1 and Layout 3 have very similar thermal performance in T_{max} and ΔT, indicating that the extreme temperatures occur in similar regions and the discrete distribution of the batteries exhibits certain similarities. This work reveals that the staggered arrangement reinforces the air-cooled effect. The overall cooling performance is similar to that of the aligned arrangement, but if the air-cooled effect is intensified, the cooling performance of the staggered arrangement would be superior. However, the staggered arrangement has longer air flow path and lower space utilization than the cross and aligned arrangement.

3.5. *The optimal arrangement of hybrid battery*

As shown in Fig. 13, aligned arrangement has the lowest ΔT and T_{max}. Among these layouts in aligned arrangement, Layout 1 has the lowest T_{max}, while Layout 5 has the lowest ΔT.

The temperature staggered-section at half the height of the batteries is calculated to explore the most effective cooling layout in the aligned

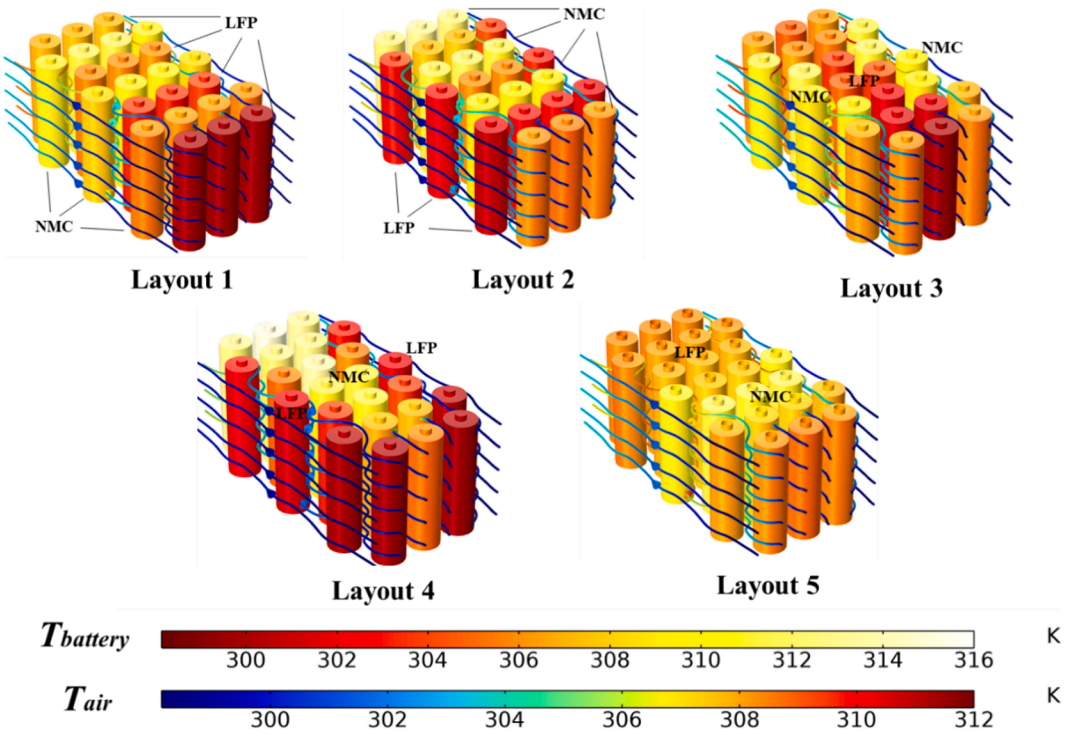

Fig. 11. Hybrid battery temperature distribution of staggered arrangement.

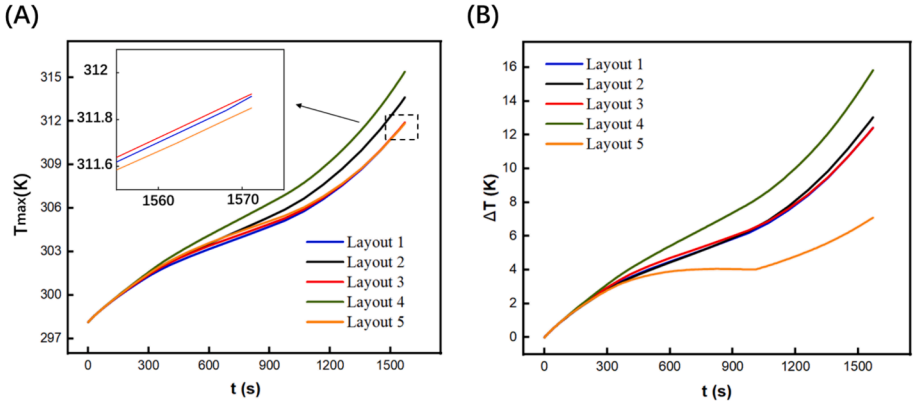

Fig. 12. Temperature-time graph curves of staggered arrangement Layout 1 ~ 6, (A) maximum temperature of battery system (T_{max}); (B) maximum temperature difference (ΔT) of battery system.

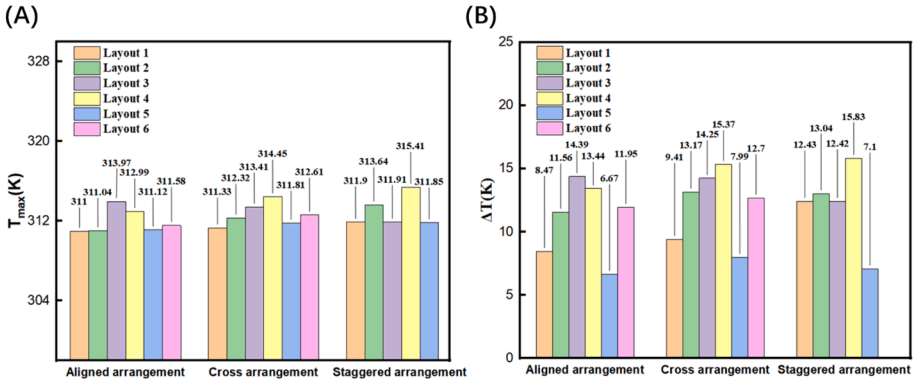

Fig. 13. (A) Maximum temperature (T_{max}) of all arrangements; (B) Maximum temperature difference (ΔT) of all arrangements.

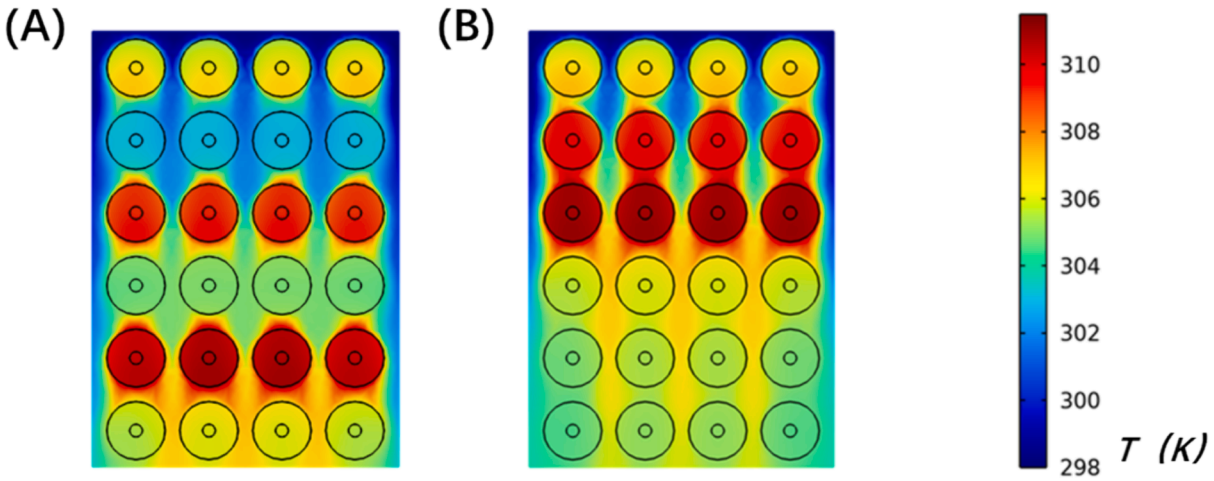

Fig. 14. Temperature field and flow field distribution of aligned arrangement, (A) Layout 1 of the aligned arrangement, (B) Layout 5 of the aligned arrangement.

arrangement, Layout 1 and 5. As shown in Fig. 14 A and B, the staggered-sectional diagram indicated the third and fifth rows of Layout 1, the second and third rows of Layout 5 are most prone to thermal runaway. The Layout 5 has a more uniform temperature, while the second row of Layout 1 has excessive cooling, leading to a larger ΔT.

Fig. 14 indicates that in the first two rows of the aligned arrangement, air-cooled is relatively effective, while the air temperature distinctly increased in the last four rows, reducing air cooled efficiency. Based on this conclusion, we propose a new layout of the aligned arrangement to optimize air-cooled structure: the first, second, and fourth rows in the air inlet direction are placed with NMC batteries, and the third, fifth and sixth rows are placed with LFP batteries, as shown in Fig. 15A. Fig. 15B shows the T_{max} and ΔT in this layout, and Fig. 15C shows the temperature staggered section at half the height of the batteries. In optimized arrangement, the T_{max} is 310.83 K, and the ΔT is 6.27 K. It is a reduction of 0.17 K compared to the minimum T_{max} of the above arrangement and a reduction of 0.4 K compared to the minimum ΔT of the above arrangement. As shown in Fig. 15C, the optimal arrangement has a higher degree of battery temperature averaging, effectively reducing the complexity of BTMS and the risk of thermal runaway.

To validate the superiority of our designed hybrid battery, simulated comparisons of the optimized hybrid battery pack with NMC battery packs and LFP battery packs are conducted under the same conditions. Through optimizing the layout design, the hybrid battery pack increased 41.7 % power density of uniform LFP battery pack and reduced 3.65 K of the maximum temperature of uniform NMC battery pack, as shown in Fig. 16.

This indicates that by combining LFP batteries with NMC batteries, the battery pack can strike a balance between high-performance output and enhanced safety and stability. Specifically, the high power and high voltage output characteristics of NMC batteries are preserved to ensure that the system meets the requirements of high-intensity applications. Meanwhile, the integration of LFP batteries plays a crucial role in improving the safety and stability of the entire battery pack. This strategic combination enables hybrid battery packs to achieve high-performance commitments while minimizing the risk of overheating and potential thermal events, ensuring safer and more reliable energy storage solutions.

4. Conclusion

In this work, we develop a hybrid battery pack, probed a corresponding SOC management method and designed an optimized thermal management system. Comparing the performance of different hybrid pack arrangements reveals that the battery layouts and battery's heat generation have a notable impact in enhancing the safety and performance of the battery pack. Among these arrangements, the aligned arrangement exhibits the most effective cooling effect, due to its shorter flow path minimizes air energy loss and reduces pressure drop.

After analyzing various arrangements, we find that avoiding the placement of NMC batteries near the air outlet and preventing the concentration of NMC is crucial for reducing the T_{max}. At the same time, effectively utilizing the scattered distribution of LFP batteries to balance the temperature of the battery pack is crucial for reducing the ΔT. Therefore, our optimally designed arrangement, inheriting the advantages of the aligned arrangement, fully considers the balancing effect of heat generated by different types of batteries in the hybrid battery

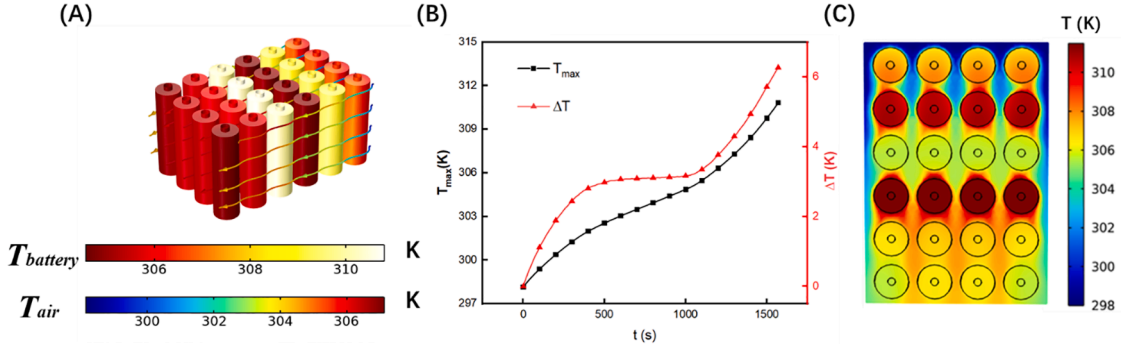

Fig. 15. (A) Hybrid battery temperature distribution of optimal layout, (B) Temperature-time graph curves of optimal layout, (C) Temperature staggered section of optimal layout.

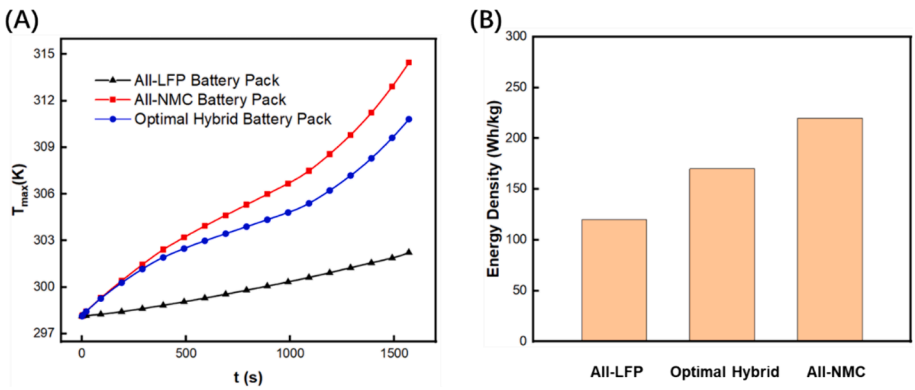

Fig. 16. Comparison of optimized hybrid battery packs with LFP battery packs and NMC battery packs (A) The maximum temperature inside the battery pack (B) The energy density of the battery pack.

group. Such optimized design leads to a higher convective heat transfer coefficient, effectively regulating the temperature to ensure optimal cooling performance. As a result, it further reduces the T_{max} and ΔT from the all arrangement.

The effects of various hybrid pack arrangements are investigated in air-cooled condition, revealing the potential benefits and challenges of utilizing hybrid battery packs. Meanwhile, the research methods and conclusions in this paper can guide the structural design of hybrid battery packs with different electrodynamic characteristics under different heat transfer conditions. The design of hybrid battery improves the energy density and enhances its safety, which effectively complements the strengths and weaknesses of NMC and LFP batteries, offering a foundation for further advancements in battery technology and thermal management strategies.

Meanwhile, this research opens several avenues for further exploration and refinement. Foremost, exploring the hybrid battery pack's behavior under dynamic operating scenarios, contributing to a deeper understanding of the system's adaptability and resilience to transient conditions. Moreover, broadening the scope to include a diverse array of battery chemistries beyond lithium iron phosphate and nickel manganese cobalt oxide can reveal new insights into the optimization of hybrid battery packs. Investigating thermal management strategies and incorporating dynamic modeling approaches to capture transient behaviors under changing conditions will enhance the system's performance over time. Pursuing these directions offers the potential to propel the development of battery technology and thermal management systems forward, leading to the realization of energy storage solutions that are not only more robust and efficient but also inherently safer and environmentally sustainable.

Author contributions statement

C.L. conceived this research. W.M. designed the work, performed simulations, analyzed the data. W.M, Y.L. H.L. and C.L organized and wrote the manuscript. All authors reviewed the manuscript.

CRediT authorship contribution statement

Wendi Mo: Writing – original draft, Visualization, Software, Methodology, Investigation, Formal analysis, Data curation. **Yiting Lin:** Writing – review & editing, Validation, Software, Methodology, Conceptualization. **Jiahui Li:** Writing – review & editing, Supervision, Funding acquisition. **Cheng Lian:** Supervision, Resources, Funding acquisition, Conceptualization. **Honglai Liu:** Supervision, Resources, Funding acquisition.

Declaration of competing interest

The authors declare that they have no known competing financial interests or personal relationships that could have appeared to influence the work reported in this paper.

Data availability

Data will be made available on request.

Acknowledgments

This work was supported by the National Natural Science Foundation of China (No. 22278127, 22378112), the Fundamental Research Funds for the Central Universities (No. 2022ZFJH004).

References

Andrea, P., Gabriele, C., Stefan, V., et al., 2019. Optimal Design of Experiments for a Lithium-Ion Cell: Parameters Identification of an Isothermal Single Particle Model with Electrolyte Dynamics. Ind. Eng. Chem. Res. 58 (3), 1286–1299.
Cao, J., Feng, J., Fang, X., et al., 2021. A delayed cooling system coupling composite phase change material and nano phase change material emulsion. Appl. Therm. Eng. 191 (2), 116888.
Chen, K., Wang, S., Song, M., et al., 2017. Structure optimization of parallel air-cooled battery thermal management system. Int. J. Heat Mass Transf. 111, 943–952.
Chen, K., Hou, J., Wu, X., et al., 2021. Design of flow pattern in air-cooled battery thermal management system. Int. J. Energy Res. 45 (6), 9541–9554.
Chen, D., Jiang, J., Kim, G.H., et al., 2016. Comparison of different cooling methods for lithium ion battery Cells. Appl. Therm. Eng. 94, 846–854.
Chen, S., Wang, Y., Wan, C., 2006. Thermal Analysis of Spirally Wound Lithium Batteries. J. Electrochem. Soc. 153 (4), 637.
Chen, Z., Xiong, R., Lu, J., et al., 2018. Temperature rise prediction of Li-ion battery suffering external short circuit for all-climate electric vehicles Application. Appl. Energy 213, 375–383.
Chiew, J., Chin, C.S., Toh, W.D., et al., 2019. A pseudo Three-dimensional electrochemical-thermal model of a cylindrical LiFePO4/graphite Battery. Appl. Therm. Eng. 147, 450–463.
Deng, J., Bae, C., Denlinger, A., et al., 2020. Electric vehicles batteries: requirements and challenges. Joule 4 (3), 511–515.
Doyle, M., Fuller, T.F., Newman, J., 1993. Modeling of Galvanostatic Charge and Discharge of the Lithium/Polymer/Insertion Cell. J. Electrochem. Soc. 140 (6), 1526–1533.
Fan, Y., Bao, Y., Ling, C., et al., 2019. Experimental study on the thermal management performance of air cooling for high energy density cylindrical Li-ion Batteries. Appl. Therm. Eng. 155, 96–109.
Fan, L., Khodadadi, J.M., Pesaran, A.A., 2013. A parametric study on thermal management of an Air-cooled Li-ion battery module for plug-in hybrid electric Vehicles. J. Power Sources 238, 301–312.
Farmann, A., Sauer, D.U., 2017. A study on the dependency of the open-circuit voltage on temperature and actual aging state of lithium-ion batteries. Power Sources. 347, 1–13.
Fuller, T.F., Doyle, M., Newman, J., 1994. Relaxation Phenomena in Li-ion-Insertion Cells. J. Electrochem. Soc. 141 (4), 982–990.
Guan, W., Bei, J., Ming, W., et al., 2023. State of charge estimation for "LiFePO4 - LiCoxNiyMn1-x-yO2" hybrid battery pack. J. Storage Mater. 69, 107345.

Guo, X., Liu, C., Li, N., et al., 2018. Electrothermal Conversion Phase Change Composites: The Case of Polyethylene Glycol Infiltrated Graphene Oxide/Carbon Nanotube Networks. Ind. Eng. Chem. Res. 57 (46), 15697–15702.
Hui, X., Minghai, S., 2021. The Control of Lithium-Ion Batteries and Supercapacitors in Hybrid Energy Storage Systems for Electric Vehicles: A Review. 45 (15), 20524–20544.
Jeon, C., Lee, Y., Kim, R., Kim, S., et al., 2023. Development of equivalent circuit model for thermal runaway in lithium-ion batteries. J. Storage Mater. 74, 109318.
Ji, C., Wang, B., Wang, S., et al., 2019. Optimization on uniformity of lithium-ion cylindrical battery module by different arrangement strategy. Appl. Therm. Eng. 157, 113683.
Ji, C., Wang, B., Wang, S., Pan, S., Wang, D., Qi, P., Zhang, K., 2019. Optimization on uniformity of Li-ion cylindrical battery module by different arrangement strategy. Appl. Therm. Eng. 157, 113683.
Kim, H., Jung, S., 2018. Battery hybridization for achieving both high power and high energy densities. Int. J. Energy Res.
Kim, T., Qiao, W., Qu, L., 2019. An Enhanced Hybrid Battery Model. IEEE Trans. Energy Convers 34 (4), 1848–1858.
Kirad, K., Chaudhari, M., 2021. Design of cell spacing in Li-ion battery module for improvement in cooling performance of the battery thermal management system. J. Power Sources 481, 229016.
Lai, X., Chen, Q., Tang, X., et al., 2022. Critical review of life cycle assessment of Li-ion batteries for electric vehicles: A lifespan Perspective. Etransportation. 12, 100169.
Li, W., Cui, H., Nemeth, T., et al., 2021. Deep reinforcement learning-based energy management of hybrid battery systems in electric vehicles. J. Storage Mater. 36, 102355.
Li, L., Dababneh, F., Zhao, J., 2018. Cost-effective supply chain for electric vehicle battery remanufacturing. Appl Energy. 226, 277–286.
Li, M., Liu, Y., Wang, X., et al., 2019. Modeling and optimization of an enhanced battery thermal management system in electric vehicles. Front. Mech. Eng. 65–75.
Li, K., Yan, J., Chen, H., et al., 2018. Water cooling based strategy for lithium ion battery pack dynamic cycling for thermal management system. Appl. Therm. Eng. 132, 575–585.
Li, S., Zhu, L., Zhang, X., et al., 2023. Recent Advances in CFD Simulations of Multiphase Flow Processes with Phase Change *Ind.* Eng. Chem. Res. 62 (28), 10729–10786.
Liao, X., Ma, C., Peng, X., Garg, A., Bao, N., 2019. Temperature distribution optimization of an air-cooling Li-ion battery pack in electric vehicles based on the response surface method. J. Electrochem. Energy Convers. Storage 16 (4), 041002.
Lu, L., Han, X., Li, J., et al., 2013. A review on the key issues for Li-ion battery management in electric Vehicles. J. Power Sources 22, 272–288.
Lu, Z., Yu, X., Wei, L., et al., 2018. Parametric study of forced air cooling strategy for lithium-ion battery pack with staggered arrangement. Appl. Therm. Eng. 136, 28–40.
Lyu, P., Huo, Y., Qu, Z., Rao, Z., 2020. Investigation on the thermal behavior of Ni-rich NMC lithium ion battery for energy storage. Appl. Therm. Eng. 166, 114749.
Mahamud, R., Park, C., 2011. Reciprocating air flow for Li-ion battery thermal management to improve temperature Uniformity. J. Power Sources 196 (13), 5685–5696.
Mahamud, R., Park, C., 2011. Reciprocating air flow for li-ion battery thermal management to improve temperature uniformity. J. Power Sources 96 (13), 5685–5696.
Maheshwari, A., Dumitrescu, M.A., Destro, M., Santarelli, M., 2016. Inverse parameter determination in the development of an optimized lithium iron phosphate - Graphite battery discharge model. J. Power Sources 307, 160–172.
Mesbahi, T., Bartholomeüs, P., Rizoug, N., et al., 2021. Advanced Model of Hybrid Energy Storage System Integrating Lithium-Ion Battery and Supercapacitor for Electric Vehicle Applications. IEEE Trans. Ind. Electron. 68 (5), 3962–3972.
Münderlein, J., Ipers, G., Steinhoff, M., et al., 2020. Optimization of a hybrid storage system and evaluation of operation strategies. Int. J. Electr. Power Energy Syst. 119, 105887.
Peng, X., Ma, C., Garg, A., et al., 2019. Thermal performance investigation of an air-cooled lithium-ion battery pack considering the inconsistency of battery Cells. Appl. Therm. Eng. 253, 596–603.
Peng, C., Ma, C., Garg, A., et al., 2019. Thermal performance investigation of an air-cooled lithium-ion battery pack considering the inconsistency of battery cells. Appl. Therm. Eng. 153, 596–603.
Ren, H., Jia, L., Dang, C., Qi, Z., 2022. An electrochemical-thermal coupling model for heat generation analysis of prismatic lithium battery. J. Storage Mater. 50, 104277.
Sato, N., 2000. Thermal behavior analysis of nickel metal hydride batteries for electric Vehicles. JSAE Rev. 21 (2), 205–211.
Shuai, Y., Guan, W., Hao, Z., et al., 2023. Equalization method of 'LiCoxNiyMn1-x-yO2 - LiFePO4' hybrid battery pack based on charging electric quantity estimation. J. Storage Mater. 69, 107959.
Tang, A., Li, J., Lou, L., et al., 2019. Optimization design and numerical study on water cooling structure for power lithium battery pack. Appl. Therm. Eng. 159, 113760.
Thien, T., Axelsen, H., Merten, M., et al., 2022. Energy management of stationary hybrid battery energy storage systems using the example of a real-world 5 MW hybrid battery storage project in Germany. J. Storage Mater. 51, 104257.
Tian, J., Wang, Y., Chen, Z., et al., 2021. An improved single particle model for lithium-ion batteries based on main stress factor compensation. J. Clean. Prod. 278, 123456.
Wang, H., Guo, Y., Ren, Y., et al., 2024. Investigation of the thermal management potential of phase change material for lithium-ion battery. Appl. Therm. Eng. 236, 121590.
Wang, L., Han, J., Liu, C., et al., 2022. State of Charge Estimation of Lithium-Ion Based on VFFRLS-Noise Adaptive CKF Algorithm. Ind. Eng. Chem. Res. 61 (22), 7489–7503.
Wang, W., He, T., He, S., You, T., Khan, F., 2021. Modeling of thermal runaway propagation of NMC battery packs after fast charging operation. Process Saf. Environ. Prot. 154, 104–117.
Wang, G., Jin, B., Wang, M., et al., 2023. State of charge estimation for "LiFePO4 - LiCoxNiyMn1-x-yO2" hybrid battery pack. J. Storage Mater. 65, 107345.
Wang, T., Tseng, K., Zhao, J., Wei, Z., 2014. Thermal investigation of Li-ion battery module with different cell arrangement structures and forced air-cooling strategies. Appl. Energy 134, 229–238.
Wu, W., Wang, S., Wu, W., et al., 2019. A critical review of battery thermal performance and liquid based battery thermal management. Energy Convers Manage. 182, 262–281.
Xu, M., Zhang, Z., Wang, X., Jia, L., Yang, L., 2014. Two-dimensional electrochemical–thermal coupled modeling of cylindrical $LiFePO_4$ batteries. J. Power Sources 256, 233–243.
Yang, X., Doyle-Davis, K., Gao, X., 2022. Recent progress and perspectives on designing High-performance thick electrodes for all-solid-state lithium Batteries. Etransportation. 11, 100152.
Yang, N., Zhang, X., Li, G., et al., 2015. Assessment of the forced air-cooling performance for cylindrical lithium-ion battery packs: A comparative analysis between aligned and staggered cell arrangements. Appl. Therm. Eng. 80, 55–65.
Zhang, X., Wang, B., Zhao, S., 2021. Oxygen anionic redox activated High-energy cathodes: Status and Prospects. Etransportation. 8, 100118.
Zhang, X., Li, Z., Luo, L., et al., 2022. A review on thermal management of Li-ion batteries for electric Vehicles. Energy 238, 121652.